

**Stress state dependency of hydrogen diffusion and embrittlement: A
new characterization program**

Jiaojiao Wu^a, Wenqi Liu^a, Eric Fangnon^a, Evgenii Malitskii^a, Pedro Vilaça^a, Junhe Lian^a *

^aAdvanced Manufacturing and Materials, Department of Mechanical Engineering, Aalto
University, Puumiehenkuja 3, 02150 Espoo, Finland

*Phone: +358 50 477 0765

junhe.lian@aalto.fi

Highlights: (maximum 85 characters per bullet point including spaces)

- The sensitivity of hydrogen embrittlement is stress states dependent.
- SH and CH have the surface crack initiation, but SDB and NDB have the central ones.
- In hydrogen environment, the quasi-cleavage fracture happens at the surface of all specimens.
- The hydrogen trapping behavior is strongly affected by the hydrostatic pressure for SH specimens.
- Stress state effect should consider dimension-induced local H content difference.

Abstract:

This study investigates the hydrogen effect on the behavior of high-strength steels under different stress states. The research is focused on tensile testing with in-situ hydrogen charging by electrochemical method. Hydrogen absorption, diffusivity, and trapping behavior are analyzed by the thermal desorption spectroscopy. Based on the finite element simulation, smooth dog-bone tensile test specimen are introduced to achieve the constant stress state until crack initiation. The focused stress states are the central-hole tension, notched-dog-bone tension, and shear. A constant loading speed with a strain rate of $10^{-4}s^{-1}$ is applied. Additional ~~tensile testing~~tests with identical setup but without hydrogen charging is conducted as the reference. The stress state ~~coupling~~dependence of hydrogen influence is characterized by the maximum force and fracture displacement. The scanning electron microscopy fractographies are employed to analyze the failure mechanisms change caused by hydrogen charging. It is proved that the hydrogen embrittlement on CP1000 steel is strongly stress-state dependent.

Keywords: Stress triaxiality; Lode angle; Hydrogen diffusivity; high-strength steel; complex-phase steel; CP1000

1 Introduction (3-5 pages)

One of the most pressing issues of the 21st century is certainly climate warming. The reduction of fossil emissions plays a key role in this multi-facet problem. Consequently, many countries, particularly in Europe, are undertaking efforts towards developing a hydrogen-based energy supply and consumption chain which is capable of matching the needs of modern mobile and industrialized societies cleanly and sustainably [1]. However, hydrogen has a significant downside for most metallic materials due to its high diffusion capability [2]. In specific, hydrogen atoms can diffuse then accumulate and interact with the matrix material, especially when defects in steel exist and then resulted embrittlement [3]. This could cause problems in hydrogen storage as well as mobile industry, most of whose material is made by AHSS. AHSS normally has a tensile strength of greater than 1000 MPa, which keep a good balance between the strength and ductility; and show a great advantage in automobile manufacturing considering weight reduction and safety factors. The manufacturing including coating process [4] introduced hydrogen in AHSS limits their utilization in car body production. Besides, [3]even for low hydrogen-concentrated applications of AHSS, such as steel manufacturing [5], period and service life time, hydrogen embrittlement (HE) is still a sensitive issue to be carefully avoided. Thus, it is significant to be researched accompanying with material development for automobile manufacturers. [6-11]

In today's automobile industry, there is a driving force in material development due to the lower CO² emissions [12]. To realize this ecological aim, light weight potential of car body constructions becomes increasingly significant [13]. Considering this potential as well as safety factors, advanced high strength steels (AHSS) show a great advantage in automobile manufacturing. The main reason is that they keep a good balance between the strength and ductility. Therefore, a reduction of wall thickness for the overall car body frame can be achieved

Commented [JL1]: Jiaojiao, I've read the introduction. The story is generally there, and I would like to give a bit new and more specific storyline that could help us to emphasize our novelty.

1. I would like you to start the story from hydrogen not AHSS, as we are going to IJHE. We shall also start from a positive side of hydrogen first with respect to the booming of hydrogen energy, hydrogen economy, etc. However, hydrogen has a significant downside for most metallic materials due to its high diffusion capability and the resulted embrittlement. This could cause problems in hydrogen production ciotn, strange and transformation and even for less hydrogen-concentrated applications, especially for high-strength steels during its production and applications. Then you could bring up your arguments in the second paragraph to give the readers an impression how important the hydrogen resistance is to AHSS in general. Here, I would like you to add 2-3 sentences on the general hydrogen embrittlement study on AHSS to show readers this is a serious matter for e.g., DP steels, TRIP steels, and especially the TWIP steels (many papers on this one).
2. This paragraph we zoom into CP steels. Your arguments are very good. Only try to add 1-2 sentences to illustrate how good their local formability is and the edge fracture resistance is. I recommend you one paper by Yuling on Materlas and Design to obtain some concrete arguments on this. Then some more specific HE study of CP steels shall be added as I commented later. I will help you to write one important sentence at the end of this paragraph to illusatate the importance of also the stress state influence of HE.
3. We will focus on the stress state influence on fracture behavior in this paragraph. I will help you write this. In includes ductile fracture and cleavage fracture and DSA.
4. This will be our strongest paragraph, basically pin-pointing the current open gaps in the hydrogen community to not systematically investigate the influence of stress states. What we need to point out is that the hydrogen crack resistance of materials is a function of h hydrogen concentration, local stress states

while maintaining its crash-worthiness [12].

however, they are susceptible to hydrogen embrittlement, depending on the embedded hydrogen contents related to stress levels and specific microstructures [12]. Regarding to the hydrogen source in automobile manufacturing industry, it can origin from steels production procedures like metallurgical melting [5] and pickling [14], car body manufacture procedures, such as welding and electrophoresis painting [15], and corrosion taken place in the service lifecycle. There are many researches indicating the HE phenomenon of first generation of AHSS, such as dual-phase (DP) steel [6, 7], transformation induced plasticity (TRIP) steel [8, 9], twinning induced plasticity (TWIP) steel [10, 11] as well as Complex Phase (CP) steel [12, 13]. –

In the first generation of AHSS, there are four typical ferrite multiphase steels: Dual Phase (DP), Complex Phase (CP), Transformation Induced plasticity (TRIP) and Martensitic (MS) steels [MAT09]. Among them, CP steels has a relative complex microstructural constituents, which

consists of bainitic ferrite with a high density of dislocations, martensite retained austenite (MA), and carbides [14]–[18, 19]. The complex phase constitution makes CP steels possessing a high strength and good toughness at the same time, which can effectively resist damage crack propagation [15] and edge fracture [16] – in ambient environment. However, manufacturing introduced hydrogen would distinctly increase the failure risk of CP steels, so HE problem became especially critical for CP steels in applications, and there is a very strong effect of the microstructure in steels on HE resistivity [17–19].

Herein, A.I. Hwang et al. [17] investigated the influence of constituent phases on the hydrogen-induced mechanical degradation in CP sheet steels. The hydrogen-induced ultimate tensile strength degradation is around 100MPa and elongation loss can reach to 70% with hydrogen charging time of 50 hours. A. Drexler et al [24], [18] studied the role of microstructure of CP steel on hydrogen susceptibility, and they found hydrogen localization within the microstructure and near plastically deformed notches result in

Commented [JL2]: Jiaojiao I suggest we shorten this part significantly into only one or max two sentences, as they are arguments everyone knows and uses.

Commented [JL3]: Jiaojiao, we need to give specific literature on the hydrogen behavior of CP steels here, either CP800, 1000 or 1200. The format shall go similar as you did for the next paragraph. We shall mentioned the names of the researchers and their main findings.

Formatted: Font: Times New Roman, 12 pt, Font color: Auto, Pattern: Clear

Formatted: Font: Times New Roman, Font color: Auto, Pattern: Clear

crack initiation. E. Malitckii et al. [19] analyzed the interaction of hydrogen with retained austenite under fatigue loading of CP1200 steels. They found that the concentration of hydrogen in steels increases with fatigue loading time, and hydrogen trapping at the α'/γ interfaces results in intergranular fatigue crack initiation. [17] Therefore, it is meaningful to continue study the failure mechanism of CP steels in hydrogen environment to instruct manufacture process improvement in an industrial aspect and understand HE mechanisms of ferritic-based steels in a research aspect.

Related to HE mechanism of steels, there are two main mechanism named hydrogen enhanced localized plasticity (HELP) [20-23] and hydrogen-enhanced decohesion (HEDE) [24-27]. Many researches have studied those mechanisms of AHSS by experiments [28-31] and simulations [27, 32, 33]. Nevertheless, only a few of studies considered the stress state influence on HE sensitivities. Díaz et al. [34] researched the local interaction between notch fracture mechanics and hydrogen diffusion behavior of high-strength steels as well as their effects of triaxiality and stress concentration on hydrogen diffusion, they found that the cohesive energy and critical separation depend both on hydrogen content and on triaxiality. In addition, Bal et al. [35] have studied the effect of hydrogen on the mechanical response and fracture locus of commercial twinning induced plasticity steels by hybrid experiments and numerical methods. They found that the deterioration in the mechanical response due to hydrogen was observed regardless of the sample geometry, and hydrogen changed the fracture mode from ductile to brittle fracture. Even though there are many studies on HE of high-strength steels, research concerning the stress state's effect on the tensile property and damage mechanism of high-strength CP steels is rare. In the current study, we focused on commercial CP1000 steel, whose tensile strength around 1000 MPa. By understanding the mechanical performance under various stress states and the HE-assistant failure mechanism of CP1000 steel, it could give a hint to other AHSS applications in the

Formatted: Default Paragraph Font

hydrogen environment, due to its complex microstructures.

Building upon the HE mechanisms on metals, in or ex situ hydrogen charging tests have been developed to quantify the HE behaviour at a structure level. In the vast number of studies in the state of the art, mostly two types of tests, standard uniaxial tensile tests [23, 30, 36] and fracture-mechanics-based tests [37, 38] have been focused on in the HE community. However, during the recent decades of research on ductile fracture, the stress states, characterized by stress triaxiality and Lode angle, have been proven to play an essential role [39-43]. Considering the dependency of hydrogen diffusion behaviour on hydrostatic pressure and plastic deformation [44, 45], it is natural to recognize the significant impact of stress states on the hydrogen-metal interaction. Therefore, a broad range of stress states from simple shear with the lowest hydrostatic pressure up to pre-cracked samples with remarkably high pressure at the crack tip will be explored in the project for HE behaviour.

This study applies the electromechanical charging method to study the hydrogen diffusivity behavior of CP1000 steel with a thickness of 1 mm. Several typical geometries of tensile specimens have been designed to cover different stress states in uniaxial tensile loading conditions. In-situ hydrogen charging uniaxial tensile testing has been carried out for CP1000 to study the hydrogen embrittlement mechanism. To quantitatively evaluate the damage property of CP1000 in an ambient or hydrogen environment, numerical simulation has been operated to find the crack initiation strain (CI) and compare the difference of CIs of CP1000 steel with or without hydrogen under various stress states.

2 Material and methods

2.1 Material

The chemical composition of the CP1000 material is performed via a BELEC LAB 3000s optical emission spectrometer. The microstructure morphology is investigated by scanning electron microscopy (SEM). By combining electron probe micro-analyzer (EPMA), electron backscatter diffraction (EBSD), nano-indentation and SEM techniques, the specific volume fraction, average grain size and aspect ratio of each phase can be derived. **Table 1** gives chemical composition of the studied CP1000 steel sheet. In addition, **Fig. 1** shows the microstructure morphology of the material, and it mainly consists of bainite, ferrite, and martensite. The phase constitution information containing volume fraction and average grain size of each phase is given in **Table 2**. The matrix phase is bainite, which possesses 73.6 % volume fraction. Moreover, ferrite and martensite possess 17.0 % and 9.0 % volume fraction in respective. Only a small amount of austenite (0.4%) are found in the material, which is difficult to be distinguished by SEM. Thus, the studied CP1000 sheet belongs to a body-centered-cubic (bcc) steel. Furthermore, the average grain size of CP1000 is about 3.4 μm , considering that of bainite, ferrite, and martensite is 4.2 μm , 1.0 μm , and 1.0 μm separately.

Table 1 Chemical composition of CP1000 steel (in wt. %).

C	Si	Mn	Ti	Cr	Mo	B
0.12	0.26	2.2	0.029	0.23	0.01	15 ppm

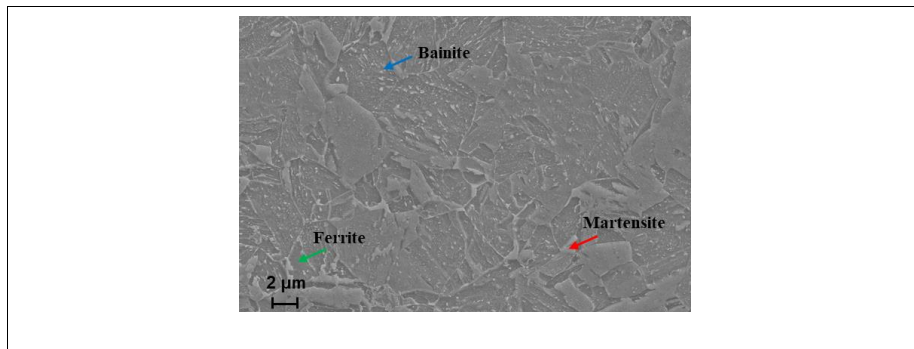


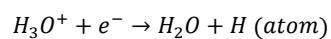
Fig. 1 The microstructure of CP1000 steel from SEM.

Table 2 Phase constitution of CP1000 steel.

Phase	Bainite	Ferrite	Martensite	Austenite
Volume fraction	73.6%	17.0%	9.0%	0.4%
Average grain size	4.2 μm	1.0 μm	1.0 μm	-

2.2 Electrochemical hydrogen charging test

In this study, hydrogen charging tests applied an electrochemical method to study hydrogen diffusivity behavior of CP1000 sheet. A glass chamber coupled with ceramic covers is designed to provide an environment for hydrogen charging reaction. Regarding to electrochemical charging reaction, there are two main components named a hydrogen charging side (the test specimen as cathode), and reference side (Pt as the anode). In addition, electrochemical solution was 3 wt. % NaCl and 0.1 wt. % NH_4SCN aqueous solution. The solution is a weak acid with a PH value around 6, which can provide H^+ in the glass chamber. Herein, steel corrosion firstly should be avoided by choosing a reasonable potential range for the H^+ reduction reaction at the cathode (tested specimen) side. The hydrogen reduction procedure of the electrochemical reaction is as



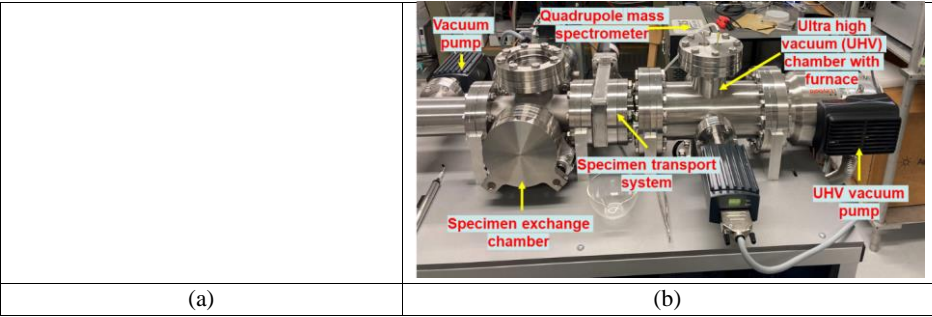
(Eq. 1.



Meanwhile, considering the efficiency and reliability of the hydrogen charging in a lab-scale condition, an optimal potential value should be selected to steadily supply H atoms diffusing into the tested specimen until a saturation state achieving. The optimal potential selection was fulfilled by dynamic potential test (DPT), which is carried out by continuously changing the electrical potential in a certain range. Followed by DPT, static potential test (SPT) was carried out by fixing the potential value as the optimal one for the whole hydrogen charging procedure. After the SPT, thermal desorption measurement (TDS) is applied to measure the hydrogen concentration in the tested specimens. The TDS apparatus was designed and constructed by Aalto University, which can measure gas pressure change in a heating furnace with ultra-high vacuum (UHV) condition. The pumping procedure of a TDS measurement, containing preliminary vacuum pumping to $1 \times 10^{-4} \text{ Pa}$ then UHV pumping to $5 \times 10^{-7} \text{ Pa}$, took around 15 minutes. After reaching the UHV condition, the furnace temperature increased from the ambient value to 1123 K with a heating rate of 10 K/min . A quadrupole mass spectrometer (QMS) sensor connected with the furnace can measure the pressure change rate caused by hydrogen escaped from the tested specimen. The measured pressure change rate at a specific temperature can be transformed to hydrogen desorption rate (HDR) with a unit of at. ppm/s. Finally, the HDR–temperature curve can be used to calculate hydrogen concentration in a tested specimen.

In hydrogen pre-charging and TDS tests, the tested specimen has a uniform dimension of $15 \text{ mm} \times 4 \text{ mm} \times 1 \text{ mm}$, which is firstly cut by electrical discharge machining (EDM) then ground to P1200 using sandpapers. The ground specimen is cleaned twice in an ultrasonic bath firstly with acetone then with ethanol for 10 minutes and air-dried before hydrogen pre-charging. Gamry Interface 1010 potentiostat was used to control the electrochemical reaction potential.

The hydrogen pre-charged specimen should be cleaned by acetone and air-dried, then weighted and transferred to do TDS within 15 minutes. QMS 100 Series Gas Analyzer from Stanford Research Systems was applied to fulfill TDS measurement. **Fig. 2** shows the illustration of hydrogen charging chamber and tested specimen, as well as TDS. To describe hydrogen diffusivity behavior of CP1000 sheet with 1 mm thickness, the charging tests were operated with different pre-charging time durations. The result was given in **Section 3.1**.



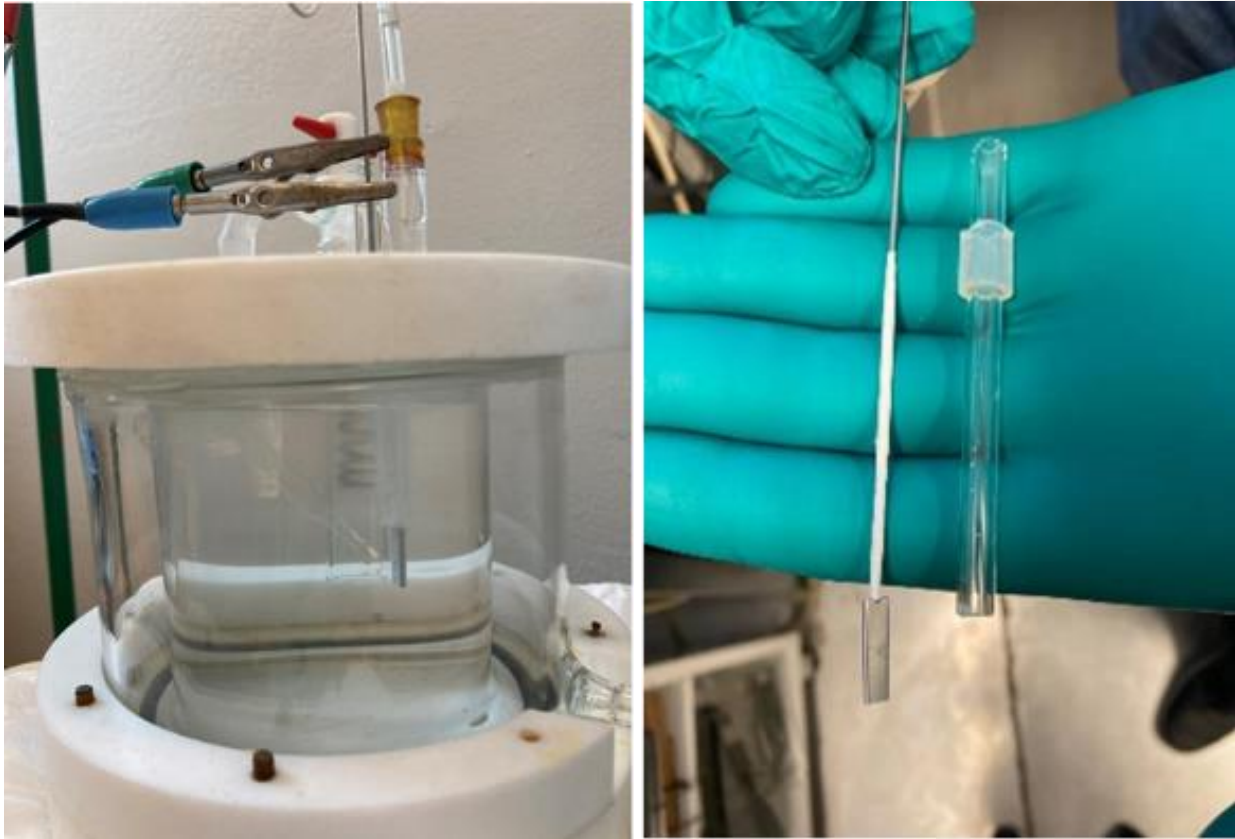


Fig. 2 (a) Hydrogen charging chamber and tested specimen, (b) TDS apparatus.

2.3 Experimental tensile test

To study the stress state's effect on CP1000 steel considering the hydrogen environment, uniaxial tensile tests were applied along the RD direction with or without in-situ hydrogen charging in this study. Tensile specimens with featured geometries were designed to meet the loading condition with various stress states. **Fig. 3** (a) shows the tensile specimen geometry with detailed features. They are the standard smooth dog-bone (SDB), a central hole with a diameter of 4 mm (CHD4), two edge notches with a radius of 40 mm (NDBR40), and two rounded eccentric positioned

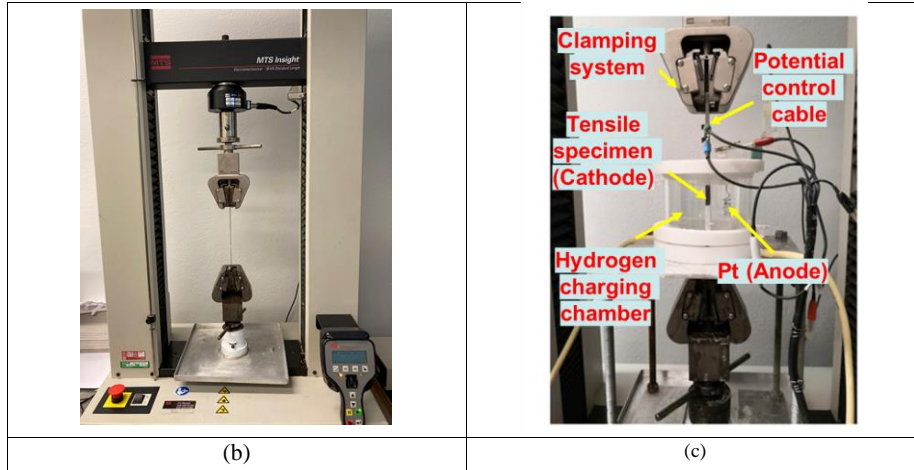


Fig. 3 Illustration of tensile specimens and tensile machine: (a) Specimen geometries (unit: mm), (b) Tensile machine, and (c) Hydrogen charging chamber coupled with test machine [46].

2.4 Numerical simulation set up of tensile test

According to the geometries of the fractured tensile specimens shown in **Fig. 3** (a), the finite element (FE) models of NDBR40, CHD4, and SH were built up by Abaqus/Explicit software for comparing stress state dependency of the studied material. Clamping regions of the tensile specimens, 25 mm away from the top and bottom edges along the tensile direction, were set as the constraint boundary conditions in the modeling. For simulating the experimental tensile constraint condition, the bottom clamping region was fully constrained in six freedom degrees, while the movement of the top clamping region was only allowed along the tensile direction without any rotation. In addition, 1/2 parts of specimens with the symmetry in thickness direction were created for a better calculation efficiency. Hence, the nodes on the z-symmetrical plane are constrained to move along the z-direction. The required displacement along the tensile direction was applied to the nodes on the top edges with a constant velocity of 0.32 mm/min for all fractured tensile specimens. Moreover, all models chose the mesh type of regular 3D brick

elements with reduced integration (C3D8R). The critical deformation regions were meshed with a 3D element size of $0.1\text{ mm} \times 0.1\text{ mm} \times 0.1\text{ mm}$, while in the transition regions, the element size gradually changed from $0.1\text{ mm} \times 0.1\text{ mm} \times 0.1\text{ mm}$ to $2\text{ mm} \times 2\text{ mm} \times 0.25\text{ mm}$. The meshed FE models with a view of in-plane zoom-in for the critical deformation zones are shown in Fig. 4.

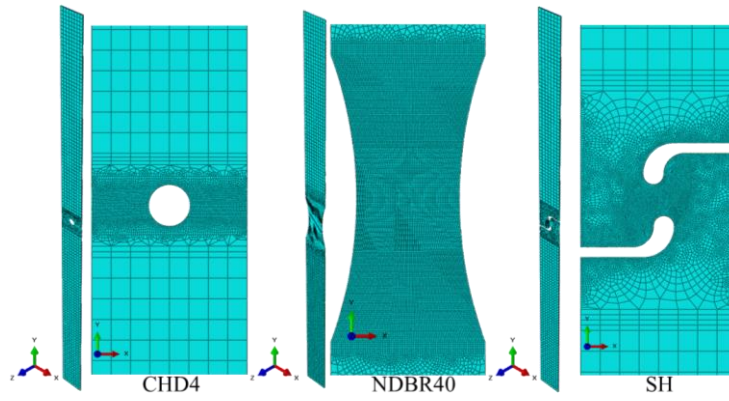


Fig. 4 FE model setup of fractured tensile specimens.

3 Results

3.1 Hydrogen diffusivity behavior

As illustrated in Section 2.2, DPT aims to choose an optimal potential for steady electrochemical hydrogen charging process. The DPT result can describe the charging current and potential relationship, which reveals the electrochemical reaction characteristics for a specific material. Fig. 5 gives the DPT measured current–potential curve for the CP1000 steel, by changing the potential from -2.4 V to -0.1 V . Basically, it describes four different stages of the electrochemical reaction. The first stage is with a potential range from -2.4 V to -1.55 V , the current decreases with it from -0.35 A to $-1.85 \times 10^{-2}\text{ A}$ with continuous changing slopes. It means that the electrochemical reaction to produce H atom is intensive but unsteady, which

may increase the risk of damaging the steel surface. The second stage is the potential range from -1.55 V to -1.41 V , the current decreases from $-1.85 \times 10^{-2}\text{ A}$ to $-5.0 \times 10^{-3}\text{ A}$ with a linear slope. It is namely the linear range, and marked as bright blue color in **Fig. 5**. It means that the hydrogen reduction reaction is mild and steady, so the risk of damaging material can be avoided. The third stage is the potential range from -1.55 V to -0.61 V , and the current continuously decreased from $-5.0 \times 10^{-3}\text{ A}$ to $-2.1 \times 10^{-7}\text{ A}$ till a sharp valley showing there. This means steel corrosion start to happen. In the following, with a potential range from -0.61 V to -0.1 V , steel corrosion gets more and more intensive, showing a continuous increase of current from $-2.1 \times 10^{-7}\text{ A}$ to -0.135 A value of -0.61 V . Thus, we chose the optimal potential of -1.41 V to do the hydrogen pre-charging test. It can provide steady, efficient, and mild reaction environment to produce H atom at the specimen surface without corrosion happening. The produced H atoms can continuously diffuse into the material, with a minimize risk of material damage, until achieving a saturation state.

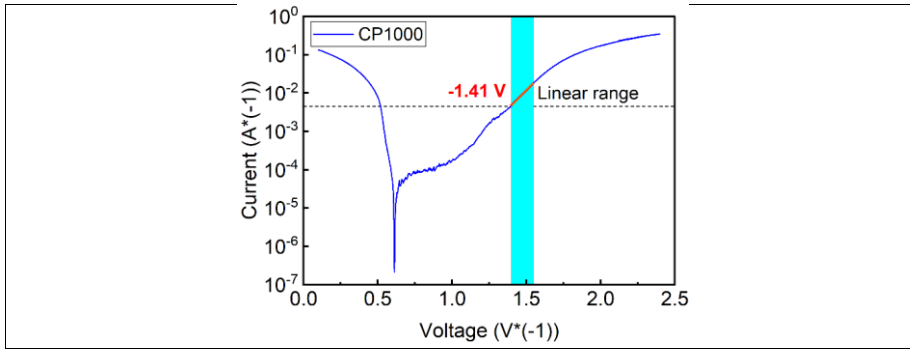


Fig. 5 Dynamic potential test of CP1000 steel.

After choosing the optimal potential as -1.41 V , hydrogen pre-charging tests were conducted to investigate the hydrogen diffusivity behavior of CP1000 steel. By setting various pre-charging times, such as 0, 2, 10, 30, 60, and 120 minutes, H concentration can be measured by TDS in respective, indicating a pre-charging time of saturation. **Fig. 6** (a) shows the HDR–temperature

curve of CP1000 steel from a TDS measurement with a pre-charging time of 30 minutes as an example to investigate the microstructural effects on hydrogen embedded in the material. There are two peaks obviously shown at the temperature of 422 K and 684 K. According to data provided by E. Viyanit [47], different activation energy of hydrogen desorption reflect different trapping sites for a specific material; normally, the lattice site has a lower activation energy level less than 10 kJ/mol while the defect sites like vacancy, dislocation, grain boundary, precipitates and so on have higher activation energy level among 20 to 100 kJ/mol. Thus, there is a deduction that, in a lower temperature range from 385 K to 460 K with a HDR peak at 422 K, the desorbed H atoms mainly belong to the lattice trapping site, while in a higher temperature range from 460 K to 1120 K with a HDR peak at 684 K, most of the desorbed H atoms are from the defect trapping sites. In addition, some sub-peaks corresponding to a specific defect trapping site can also be found from the 460 K to 1120 K temperature range in the HDR curve. They are mean to be researched and discussed in the further study.

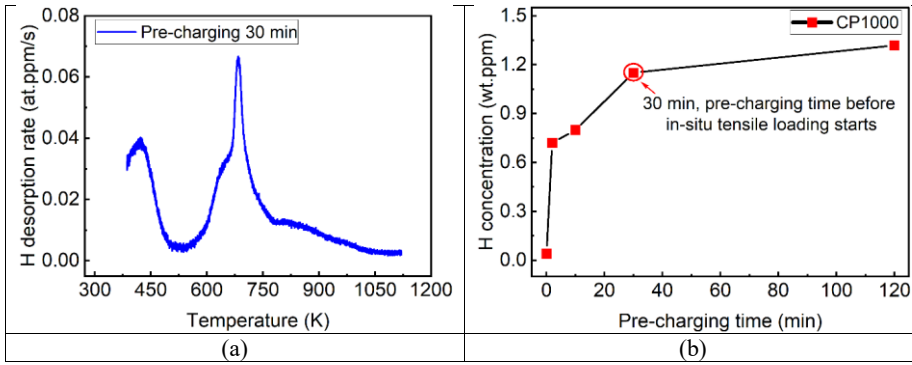


Fig. 6 Hydrogen charging parameter and related diffusivity behavior of CP1000 steel.

To describe the hydrogen diffusivity capacity in CP1000 steel, **Fig. 6** (b) shows the result of hydrogen concentration from TDS measurement. From the pre-charging time range from 0 to 30 minutes, the hydrogen concentration in the material dramatically increases but the slope is

continuously decreasing. After 30 minutes, with pre-charging time increasing, the hydrogen concentration increases very slowly until reaching a value of 1.32 wt.ppm at the 120 minutes, which is close to a saturation state, and the hydrogen concentration will not increase anymore. Considering efficiency of the in-situ tensile tests in hydrogen environment, the pre-charging time is chosen as 30 minutes before the tensile loading starts. A distinct difference of mechanical behavior between tensile experiments for CP1000 steel with or without hydrogen charging will be displayed in the next section.

3.2 Experimental tensile property with or without hydrogen charging

The results of uniaxial tensile tests of all designed specimens are presented in **Fig. 7**. The black lines represent for tensile property without hydrogen charging, while the red lines stand for that with 30 minutes hydrogen pre-charging and in-situ hydrogen-charging till final fracture. In addition, the colored area means the data scatter range among parallel tests for each loading condition. When investigating the hydrogen influence on tensile property of the material, two parameters, ultimate tensile stress or stress (UTS) and ductility (engineering strain or displacement at fracture moment), are mainly compared in **Table 3**. One thing need to be mentioned that, the minus value shown in **Table 3** when calculating tensile property parameters' reduction by H means the value is actually increased by hydrogen. As **Table 3** illustrated, concerning the average UTS and the average ductility of parallel specimens for different geometries, most of them are reduced by hydrogen; however, hydrogen's influence on ductility are much more significant than that on UTS. Specifically, for SDB and NDBR40 tensile specimens in hydrogen environment, the average UTS are almost the same, while the average ductility are respectively reduced by 25.16 % and 19.57 %; for CHD4 and SH tensile specimens in hydrogen environment, the average UTS are reduced by 3.96% and 5.82 %, while the average ductility are reduced by 25.96 % and enhanced by 15.57 % in respective. Further analysis on

hydrogen's effect on tensile property and fracture mechanism of each geometry type will be discussed in **Section 4**.

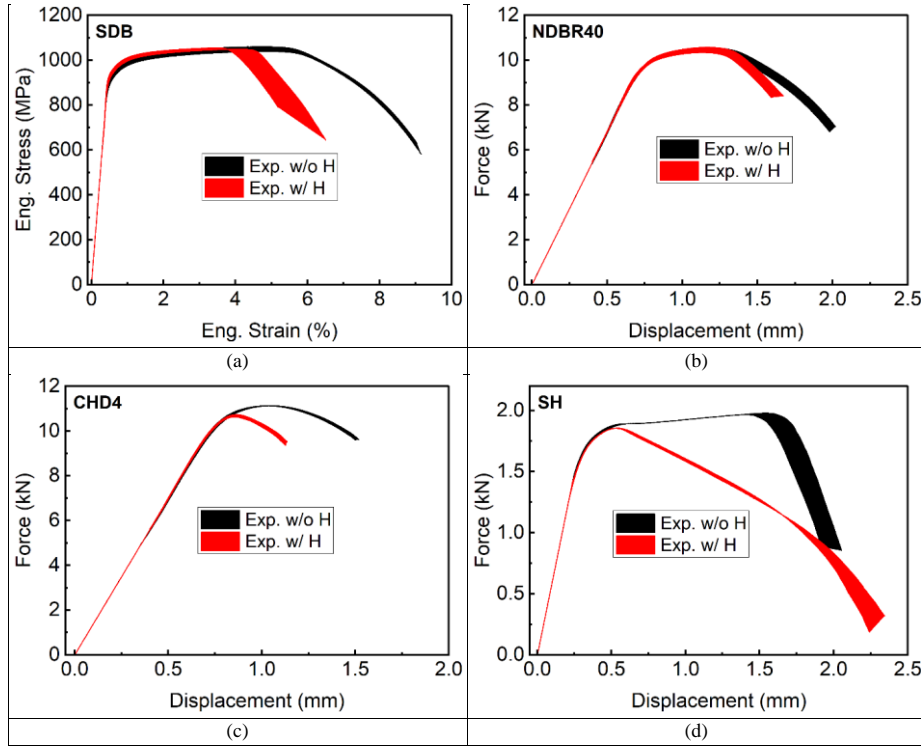


Fig. 7 Mechanical property comparison of CP1000 steel in uniaxial tensile tests with or without hydrogen charging: (a) SDB, (b) NDBR40, (c) CHD4, and (d) SH.

Table 3 Tensile property comparison of CP1000 steel without or with hydrogen charging.

Tensile property parameter		SDB	NDBR40	CHD4	SH
Avg. UTS	w/o H	1049 MPa	10.49 kN	11.12 kN	1.98 kN
	w/ H	1052 MPa	10.43 kN	10.68 kN	1.86 kN
	Reduction by H	-0.25 %	0.60 %	3.96 %	5.82 %
Avg.	w/o H	9.10 %	2.00 mm	1.51 mm	1.98 mm

Ductility	w/ H	6.81 %	1.61 mm	1.12 mm	2.29 mm
	Reduction by H	25.16 %	19.57 %	25.96 %	-15.57 %

3.3 Numerical fitting tensile property under different stress states

Based on the experimental result in tensile test of SDB without hydrogen charging, the combined Voce–Swift law, as illustrated in (Eq. 2), was applied to calibrate the flow curve of CP1000 steel till the true plastic strain of 3. Fig. 8 (a) displays the experimental flow curve as black line, and the calibrated flow curve as red dot. Then, the calibrated flow curve was employed as the hardening law of plasticity deformation in numerical simulation according to von Mises yield criterion for tensile tests of NDBR40, CHD4, and SH specimens without hydrogen charging. The corresponding experimental and simulated force–displacement curves of those specimens are separately given in Fig. 8 (b-d), which are marked as black line and red dot in respective. Results from Fig. 8 suggest that the calibrated parameters in the combined Voce–Swift law is reasonable, because the experimental and simulated force–displacement curves are fitted well with each other for all fracture specimens. Thus, the simulation results for all fracture specimens based on the calibrated flow curve can be used to predict their tensile loading history until crack initiation happening. Furthermore, stress state related parameters such as the stress triaxiality and the Lode angle parameter can be characterized according to [43] and [48].

$\bar{\sigma}_y = 0.8 \times \left(922.8 + 162.0 \times (1 - e^{-52.86 \times \bar{\epsilon}_p}) \right) + 0.2 \times \left(1254 \times (5.13 \times 10^{-5} + \bar{\epsilon}_p)^{0.051} \right)$	(Eq. 2)
---	---------

Where $\bar{\sigma}_y$ is the flow stress and $\bar{\epsilon}_p$ is the equivalent plastic strain (PEEQ).

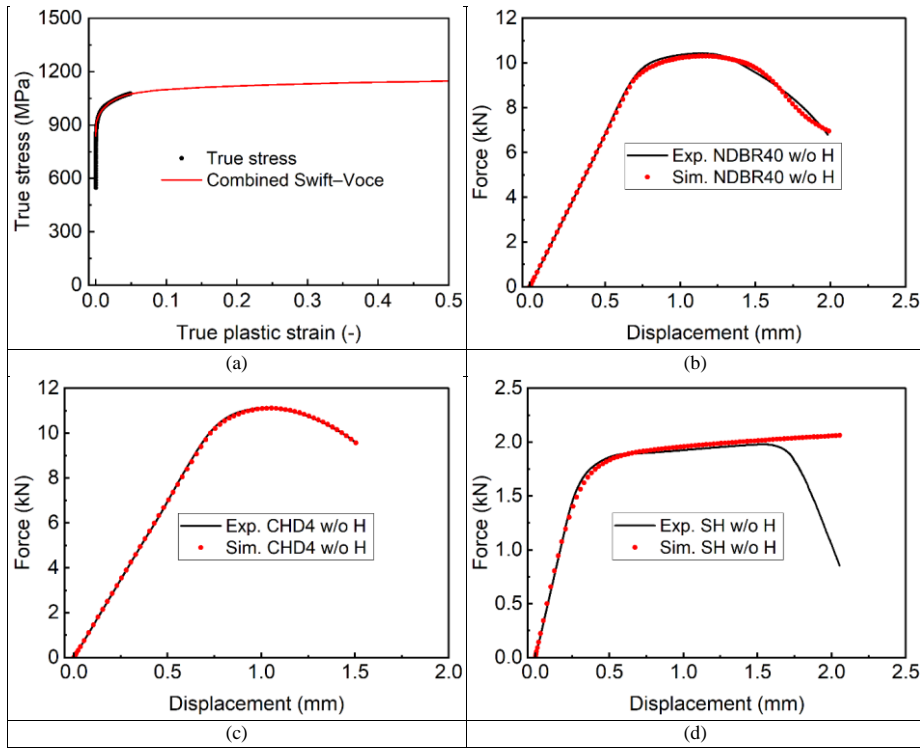


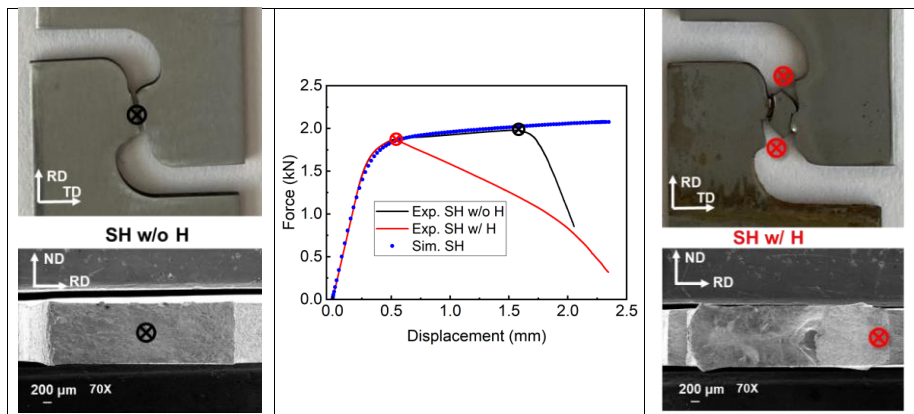
Fig. 8 (a) Flow curve calibration based on the combined Swift–Voce law; (b, c, and d)

Experimental and simulated tensile results for NDBR40, CHD4, and SH specimens without hydrogen charging.

4 Discussion

4.1 Crack initiation determination

In a tensile test, determining the moment when and the location where crack initiation (CI) happened is important to understand stress state's and hydrogen's influences on tensile property of CP1000 steel. Combining the experimental and simulated results, CI determination can be achieved by following principles. For tests without hydrogen charging, a CI moment is defined when a variation observed between the experimental and simulated force–displacement curves, and a CI location is defined as a place possessing maximal equivalent plastic strain (PEEQ). They are marded as black symbols in



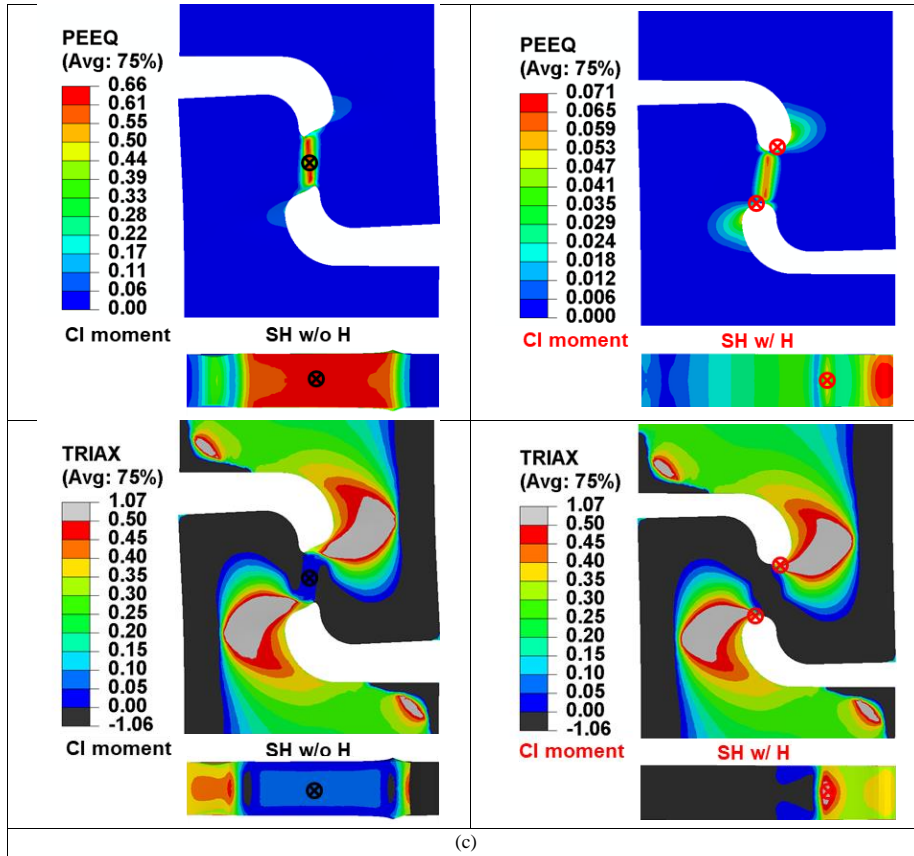
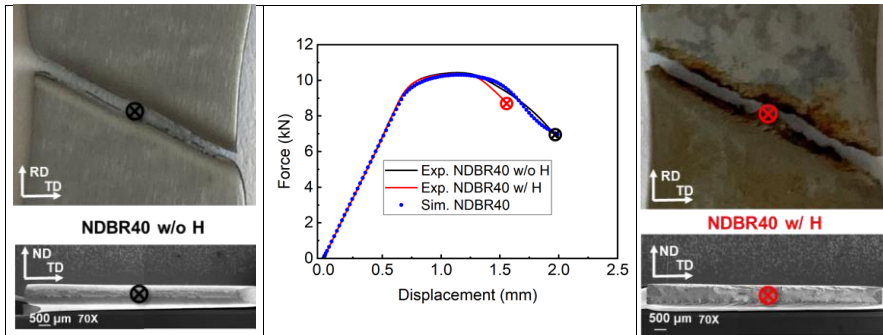


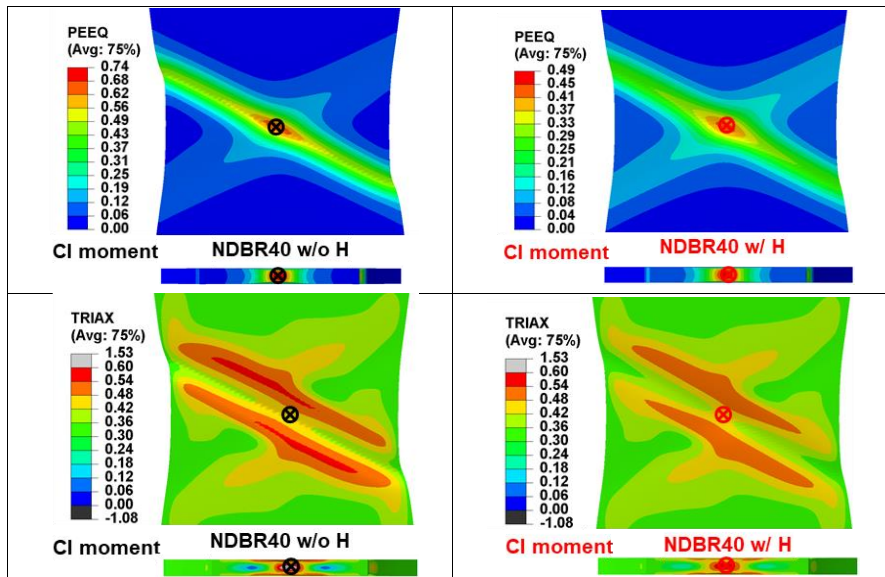
Fig. 9. According to this principle, the CI moment of NDBR40 and CHD4 specimens both happen at the final fracture moment, and that of SH specimen happens at the force drop occurrence; Meanwhile, the CI locations of NDBR40 and SH specimens are in the center of the fracture surface, and that of CHD4 specimen is nearby the hole of the fracture surface.

Nevertheless, for tests with hydrogen charging, the determination of CI, which marked as red symbols in **Fig. 9**, might deviate from the previous principles to some extent. In one hand, even though the CI moment occurs earlier than specimens without hydrogen charging due to the HE mechanism, their response to hydrogen's influence are different under various stress states. In the other hand, the CI locations cannot be only determined according to the PEEQ. Herein,

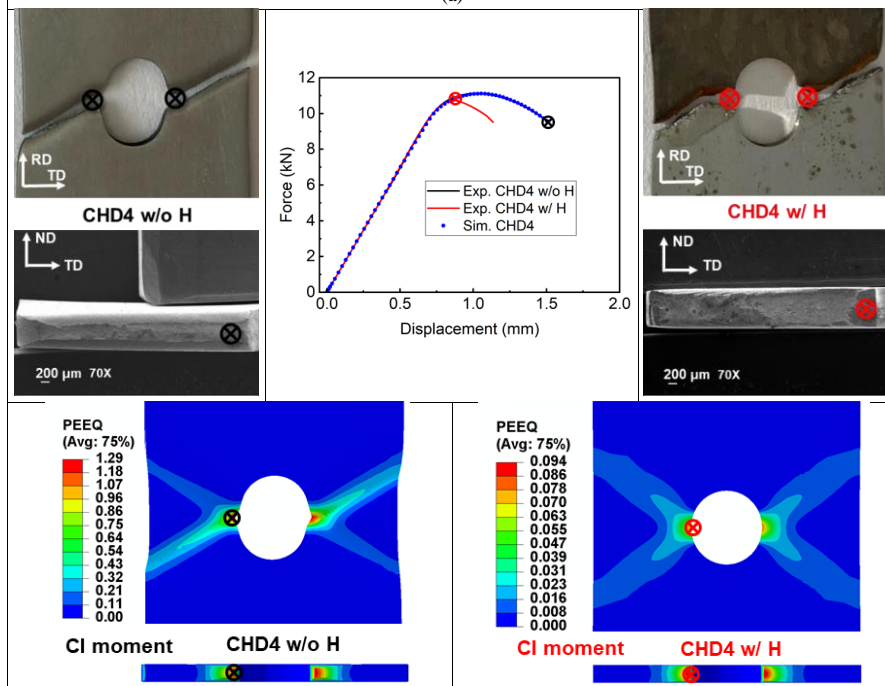
stress triaxiality as another critical factor needs to be considered as well. The reason is that various stress states may lead to variations of hydrogen concentration and distribution in specimens during the in-situ hydrogen charging tensile test. A higher stress triaxiality corresponds to a primarily hydrostatic stress state, which promote a tendency of HE. In another word, the higher stress triaxiality is, the higher HE tendency is. Thus, a CI location might be shown at a place with a higher stress triaxiality, even though the PEEQ there is not in the maximal value. On the basis of above illustration, for NDBR40 specimen, the CI moment with hydrogen charging is still at the final fracture moment. Herein, the force drop caused by hydrogen charging in experiments happens in the necking stage, and the divergence is too small to be ignored. Thus, the final fracture moment of NDBR40 is also treated as the deviation starting point between experimental and simulated force–displacement curves. Considering the CI location, it is still defined as the center on the fracture surface, because the central element holds the highest PEEQ and stress triaxiality until the CI moment. For CHD4 specimen, the CI moment is determined as the divergence between experimental and simulated force–displacement curves, which is also the moment when maximal force displaying. Herein, the force drop in experimental curve induced by hydrogen can not ignored, because it happens during the plastic deformation in advance of maximal force point. In addition, hydrogen influence on CI location makes it shift a little bit from the nearby site to the edge site of the hole. The reason might be that hydrogen would diffuse from the hole surface along TD direction as well as from the specimen surface along ND direction. Hence, more hydrogen atoms accumulate at the nearby and the edge sites of the hole and enhance its HE tendency altogether. The flat platform observed from experimental fracture samples confirm this deduction. For SH specimen, the CI moment is defined as the experimental force drop occurrence, which shows up much more early comparing to the specimen without hydrogen charging. It is noted that the CI location of SH specimen moves from

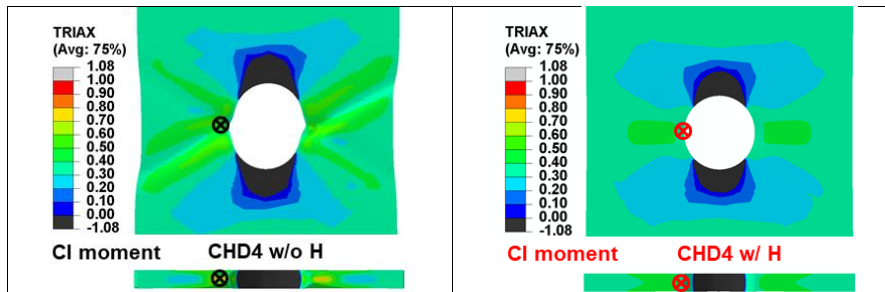
the center on the symmetry plane in the shear region to the edge site of the central half-round grooves. The reason of the CI location shifting is similar to that of CHD4 specimen but the HE tendency is stronger here, because hydrogen accumulation becomes more concentrated on the edge site than that happens in CHD4 specimens. In specific, the hole edge site of CHD4 specimens has a tension stress state (with a positive stress triaxility value marked as green color band), while for SH specimens, the edge site of the central half-round grooves has a compression stress state (with a negative stress triaxility value marked as dark color band). As a result, the absorbed hydrogen atoms tend to diffuse from a compression to a tension stress state. In another word, SH specimens go through hydrogen accumulations at the edge site of the central half-round grooves from two perspectives. In one hand, the edge site absorbs more hydrogen from the environment during the in-situ hydrogen charging tensile tests; in another hand, it absorbs more hydrogen from the inner region due to different stress states. Furthermore, the shift of CI location in SH specimen change the stress state of the shear region as well as the crack propagation path. In summary, hydrogen's influence on CI moment and locations under various stress state of CP1000 steel is significant. The further analysis of stress state dependency on tensile property of the material with or without hydrogen charging is discussed in **Section 4.2**.



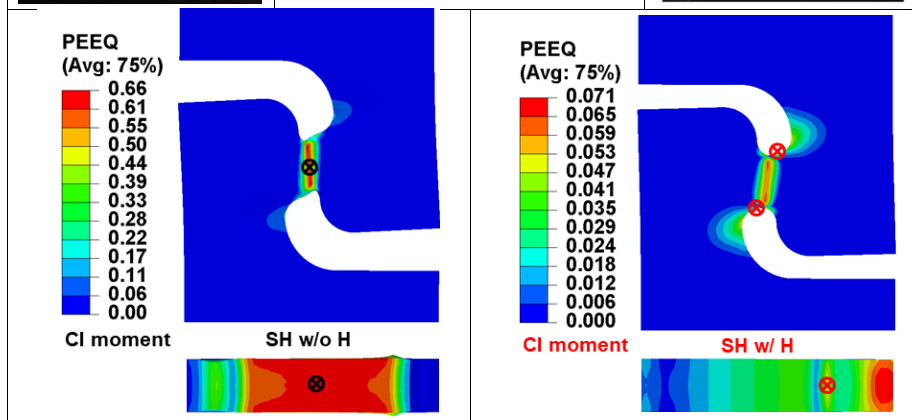
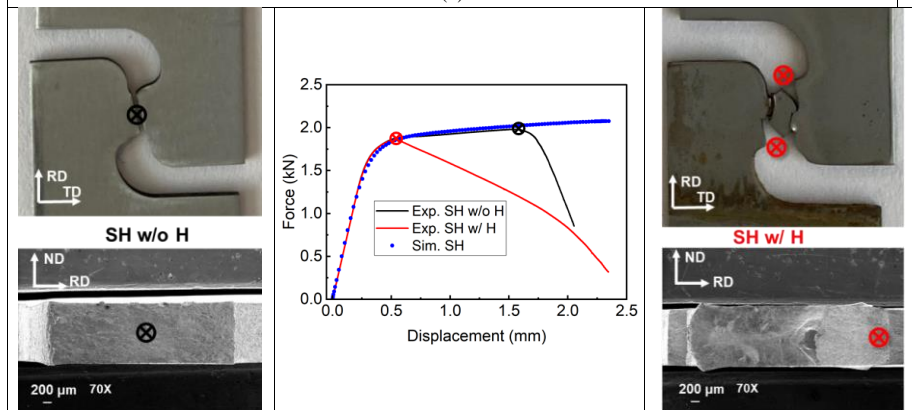


(a)





(b)



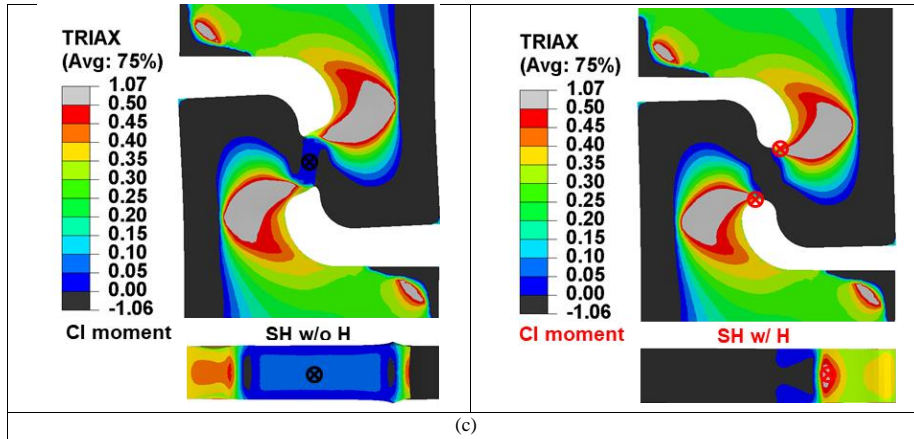


Fig. 9 Crack initiation determination of CP1000 steel during tensile tests: (a) NDBR 40, (b) CHD4, and (c) SH. (First row: real fracture sample for tests without H, tensile force–displacement curves, real fracture sample for tests with H; Second row: Simulated fracture pattern of equivalent plastic strain at CI moment for tests without H and with H; Third row: Simulated fracture pattern of stress triaxiality at CI moment for tests without H and with H).

4.2 Stress state dependency on tensile property

As referred to as CI locations in **Section 4.1**, the critical elements of the fracture specimens in FE modeling are selected to investigate the tensile properties' dependency on stress states with or without hydrogen charging. As **Fig. 10** (a) illustrating, the critical elements in FE modeling are the central element of NDB40 specimens (marked as green square), central element on the hole edge of CHD4 specimens (marked as blue square), the central element on the symmetry plane in the shear region of SH specimens without hydrogen charging (marked as black square), and the central element on the half-round groove edge in the shear region of SH specimens with hydrogen charging (marked as red square). For each type of specimens, the hardening law, boundary conditions, and the loading history of the critical elements are the same for simulations with or without hydrogen charging.

Fig. 10 (b-c) show the loading paths of the critical elements for fracture specimens, and the PEEQ changes with stress state parameters, the stress triaxiality and Lode angle parameter, are focused to discuss. Specially, due to the change of critical elements for SH specimens in tensile tests by introducing hydrogen, they are respectively named by SH_shear (in tests without hydrogen charging) and SH_edge (in tests with hydrogen charging) to distinguish from each other. It is observed that CHD4 and NDBR40 specimens both have non-proportional loading paths (marked as blue and green colors in respective), and their loading paths keep as the same no matter in tests with or without hydrogen charging. Meanwhile, SH_shear and SH_edge holds nearly proportional loading paths (marked as black and red colors in respective), if ignoring the unstable variation in the initial loading stage. Different from CHD4 and NDBR40 specimens, the loading path of SH specimen changed with the critical element shifting by introducing hydrogen. Concerning stress state parameters of a critical element, the stress triaxiality defines the fracture modes like ductile or brittle fractures, and the Lode angle parameter defines the deformation categories as pure tension, shear, pure compression, and mixtures of shear-tension or shear-compression. For SH_shear, both stress triaxiality and Lode angle parameter are close to zero during the whole loading history; in contrast, those parameters for SH_edge both increase to around an average value of 0.5. It suggests that the critical elements of SH specimens go through a transition from a pure shear deformation to a mixed shear-tension deformation under the effect of absorbed hydrogen. Besides, their fracture modes are both ductile fractures; however, the fracture characteristics tends to transform from shear slipping to a mixture of shear slipping and dimples formation. In addition, for CHD4 and NDBR40 specimens, the Lode angle parameter of the previous one is near 1.0 which is close to a pure tension deformation during the whole loading, while the latter one holds a transition from near pure tension to mixed shear-tension deformation. Furthermore, the stress triaxiality of NDBR40 specimens are in the range from 0.36 to 0.67,

which holds the largest level among all fracture specimens; and that of CHD4 has a range from 0.35 to 0.57 which is not much different from NDBR40. Possessing those values of stress triaxiality, both of CHD4 and NDBR40 specimens are ductile fractures, with the fracture characteristics of a mixture of shear slipping and dimples formation.

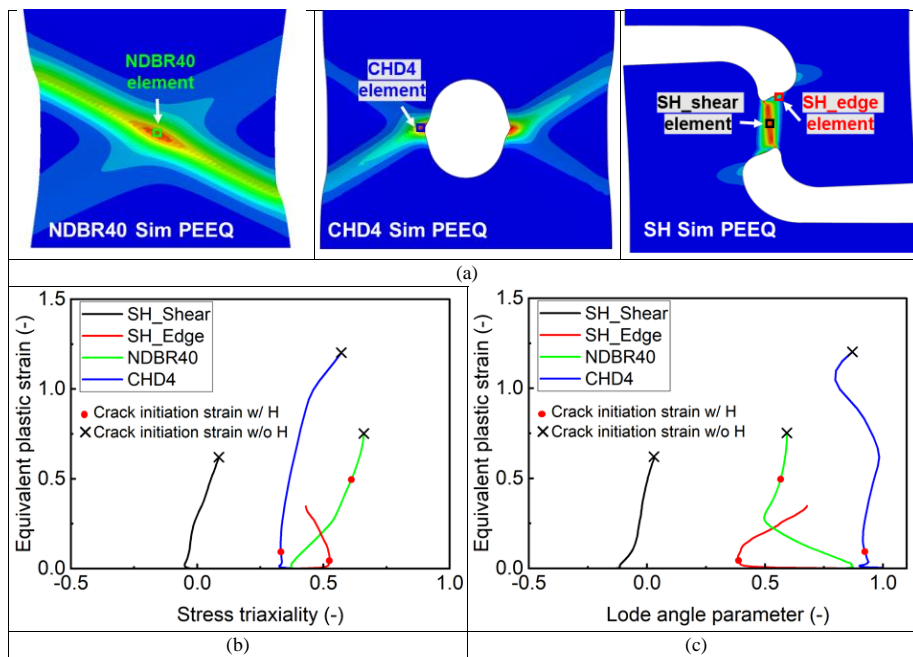


Fig. 10 (a, b) Loading paths of the critical elements of CHD4, NDBR40, and SH specimens, (c, d) critical initiation element of SH, and CHD4 specimen.

Except the loading paths, stress state parameters and PEEQ at CI moment with or without hydrogen charging (marked as red or black crosses in respective in **Fig. 10** (b-c)) are selected in **Table 4** to discuss the hydrogen's influence on them. There is a result that at CI moment, the hydrogen influence on stress triaxiality and Lode angle parameters of different types of specimens are quantitatively different from each other. In detail, both the two parameters of

NDBR40 has seldom been affected by hydrogen at CI moment while SH has a total reversed result, and the hydrogen's effect on those parameters of CHD4 are in between. Moreover, regarding to the PEEQ at CI moment (critical PEEQ), the CP1000 steel has a good crack resistance without hydrogen charging for all of the critical PEEQs are larger than 0.5. Nevertheless, hydrogen results in the distinctly reduction of critical PEEQs of all specimens, which is consistent with a result in **Section 3.2** that hydrogen induces ductility shortence of CP1000 steel in tensile tests. results. Nevertheless, the hydrogen's influence on PEEQ are also quantitatively different for different type of fracture specimens. When comparing the critical PEEQ of specimens with or without hydrogen charging, NDBR40 has been reduced by 33.3% while those of CHD4 and SH have been decreased by more than 92%. Herein, the huge diffenrence of critical PEEQ reduction by hydrogen between NDBR40 and the other two types of specimens may relate to their CI locations. In in-situ hydrogen charging tensile tests, the CI location of NDBR40 is still in the center of the specimen, while those of CHD4 and SH are in the edge of the specimens. Hydrogen accumulation near the edge site enhances specimen's HE tendency, which results in a dramatic reduction of critical PEEQ for CHD4 and SH specimens.

Table 4 Stress state parameters and PEEQ at crack initiation moment of fracture specimens

Sample name		Stress triaxiality, -	Lode angle parameter, -	Equiv. plastic strain, -
NDBR40	w/o H	0.66	0.59	0.75
	w/ H	0.61	0.57	0.50
	Reduction by H			33.3%
CHD4	w/o H	0.57	0.87	1.20
	w/ H	0.33	0.92	0.094

Reduction by H				92.2%
SH	w/o H, shear element	0.085	0.030	0.62
	w/ H, edge element	0.52	0.39	0.044
	Reduction by H			92.9%

In summary, the influence of stress states on the hydrogen embrittlement of CP1000 steel cannot be ignored, however, the current FE modeling strategy is difficult to accurately predict the fracture locus of CP1000 steel in hydrogen environment. There might be some reasons are: firstly, the traditional designed geometries may have drawbacks to assure a steady stress state in hydrogen environment, especially the SH specimen, which can not keep a pure shear deformation during the whole loading; secondly, local hydrogen concentration and distribution within specimens cannot be tracked by simulation during the in-situ hydrogen charging tensile tests; thirdly, the current modeling is only based on the smooth uniaxial tensile testing, so the stress state range is limited to predict the whole fracture locus of the material considering the effect of HE. The calibration of the stress-state informed HE fracture locus is necessary. Therefore, some improvements are recommend for further study. First of all, establishing a coupled hydrogen diffusion and deformation model to predict in-situ synchronous local stress state and hydrogen distribution fields. In addition, designing new geometries to fit the purpose of stress state assurance in hydrogen environment. Moreover, designing more geometries for different types of mechanical tests to involve more stress states for a full-range fracture loci calibration, no matter for with and without hydrogen charging.

4.3 Failure mechanism without or with hydrogen charging

In previous section, the stress state dependency of CP1000 steel's tensile performance with or without hydrogen charging is discussed. In this section, failure mechanism of the studied material with or without hydrogen charging under various stress states are specially investigated. Firstly,

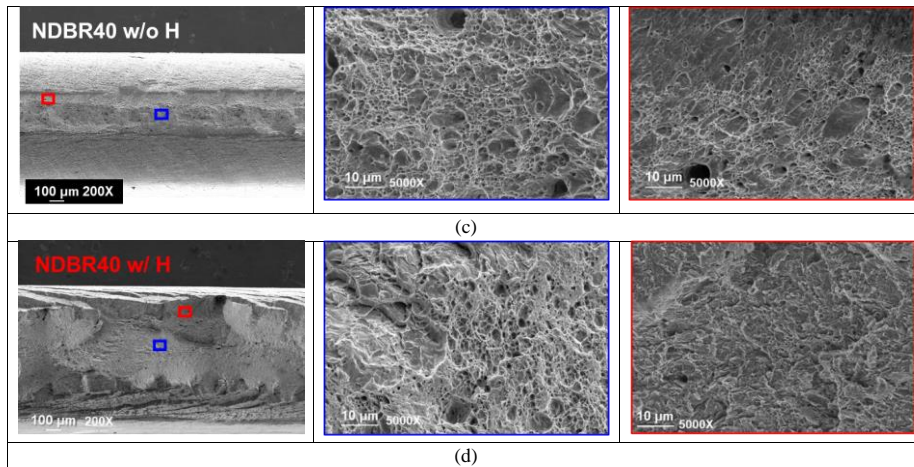


Fig. 11 shows the tensile fractography of SDB and NDBR40 specimens with and without hydrogen charging. Because their CI locations are both in the center, so the central region of the specimens are illustrated to discuss. For SDB specimens without hydrogen charging, as

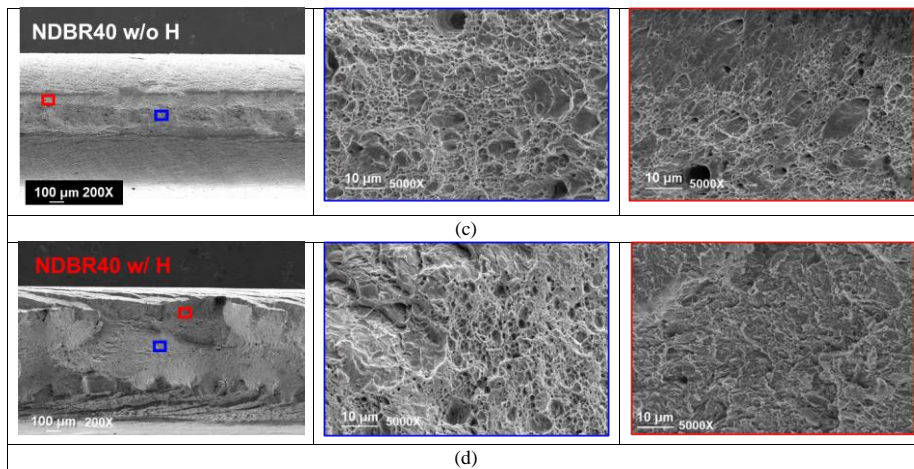


Fig. 11 (a) displaying, the specimens go through an obvious necking in thickness direction, and a lot of dimples are found in the central region. Thus, the failure mode of SDB specimens without hydrogen charging is determined as a typical ductile fracture. For SDB specimens with hydrogen charging, as shown in

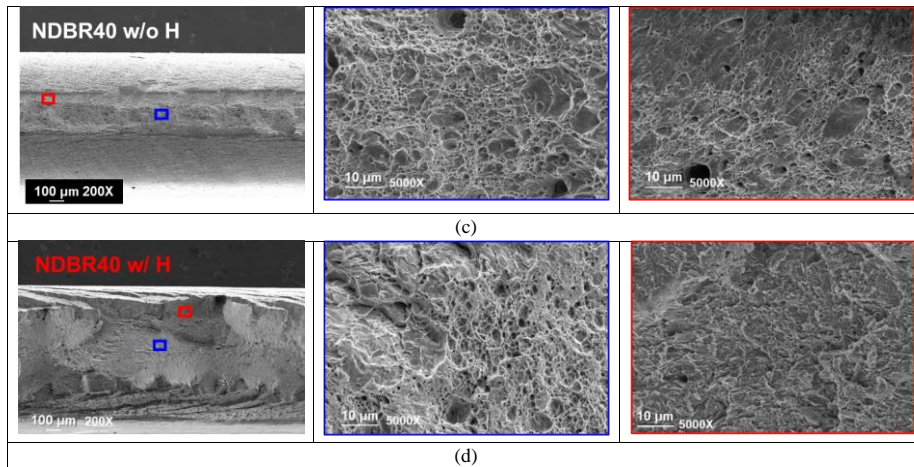


Fig. 11 (b), some micro-cracks show up in the necking region and the necking in thickness direction of the specimen is obviously weakened. In addition, the dimples in the central region become smaller and shallower. Therefore, even though the failure mode of SDB specimen with hydrogen charging is still ductile fracture, its ductility is reduced by hydrogen. NDBR40 specimens have the similar results as SDB specimens, as shown in

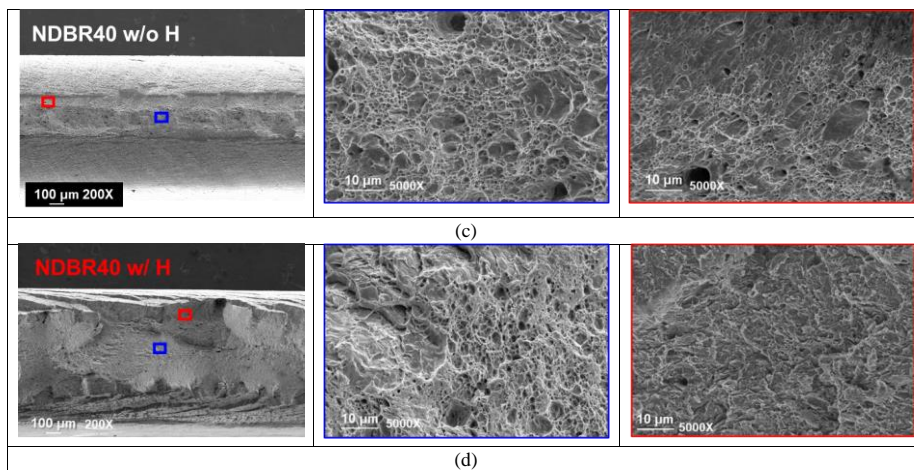


Fig. 11 (c-d). No matter to observe the central (marked as blue square) or edge (marked as red square) sites of NDBR40 specimens, both of the failure characteristics are dimples, and the

hydrogen charging only makes those dimples smaller and shallower rather than change the fracture mode.

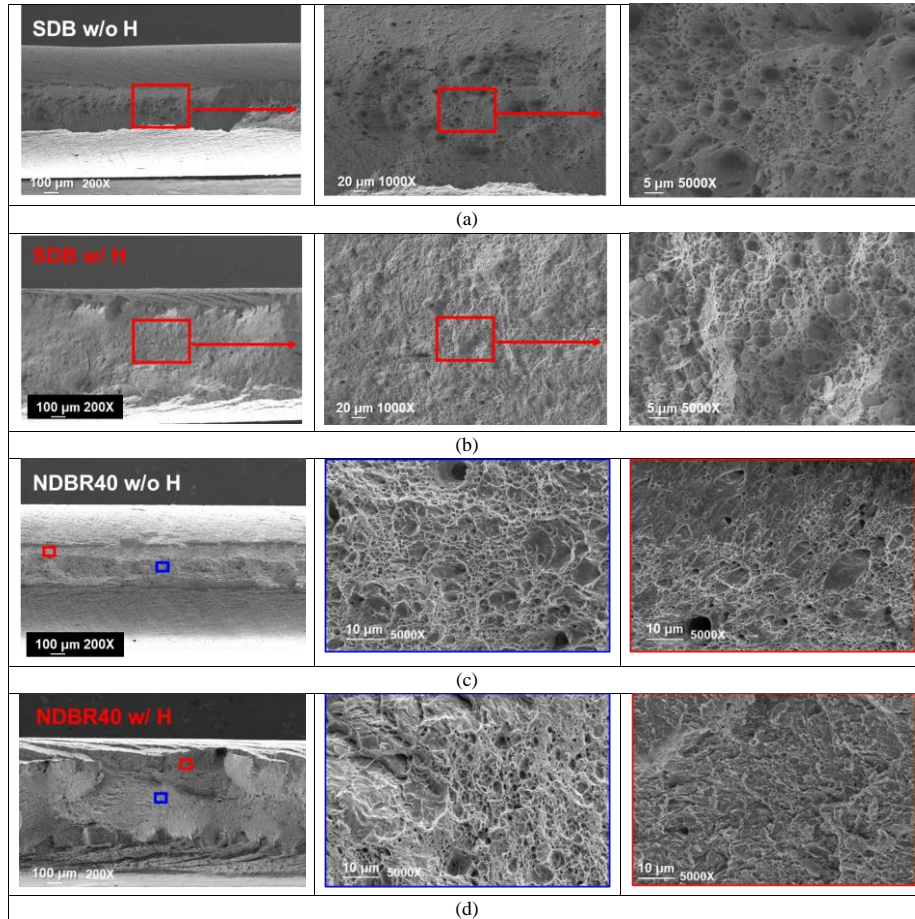
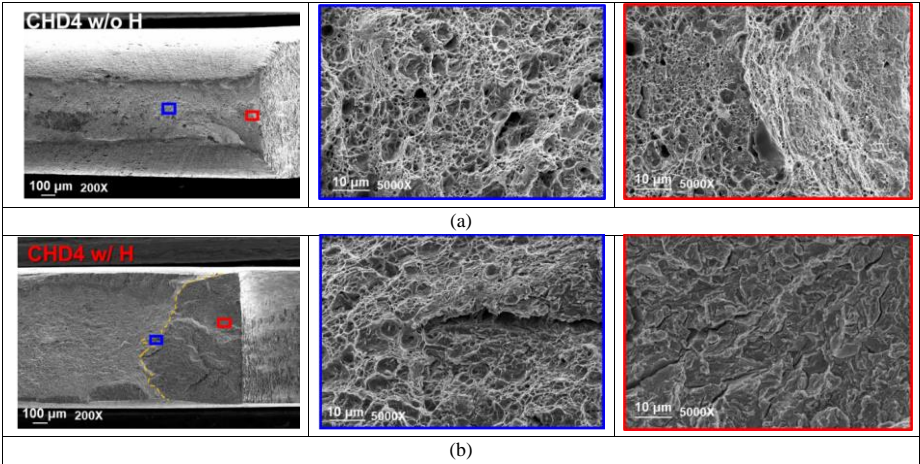


Fig. 11 Tensile fractography in the central site: (a-b) SDB specimens without and with hydrogen charging, and (c-d) NDBR40 specimens without and with hydrogen charging.

In the following, **Fig. 12** shows the tensile fractography around the CI locations of CHD4 and SH specimens with and without hydrogen charging to investigate their failure mechanisms. As **Fig. 12** (a) shown, for CHD4 without hydrogen charging, necking are observed in thickness

direction and dimples are found both at the edge (marked as red square) and near-edge (marked as blue square) sites of the hole, so it is ductile fractures. However, the charged hydrogen change the fracture mode of CHD4 specimens. For near-edge site, it still shows dimples as characteristics of ductile fracture mode, while at the hole-edge site, river flow patterns as well as very shallow dimples appear at the same time, as shown in **Fig. 12** (b). This type of features is referred to as the quasi-cleavage fracture characteristics. It suggests that the hydrogen concentration near the CI location can aggravate the HE tendency of the studied material. Similar to the CHD4, SH specimens also go through a fracture mode transition from ductile fracture to quasi-cleavage fracture induced by hydrogen at the edge site of the shear-grooves. It is noticeable that, without hydrogen charging, SH has a uniform deformation characteristics of shear slipping on the whole fracture surface. In contrast, except from the site near the shear-grooves has a quasi-cleavage fracture feature, the other region on fracture surface of SH specimens has mixed features of shallow dimples and shear slipping. This coincides with the stress state transition from a pure shear deformation to a mixture of tension-shear deformation considering hydrogen's influence, as previous section discussed.



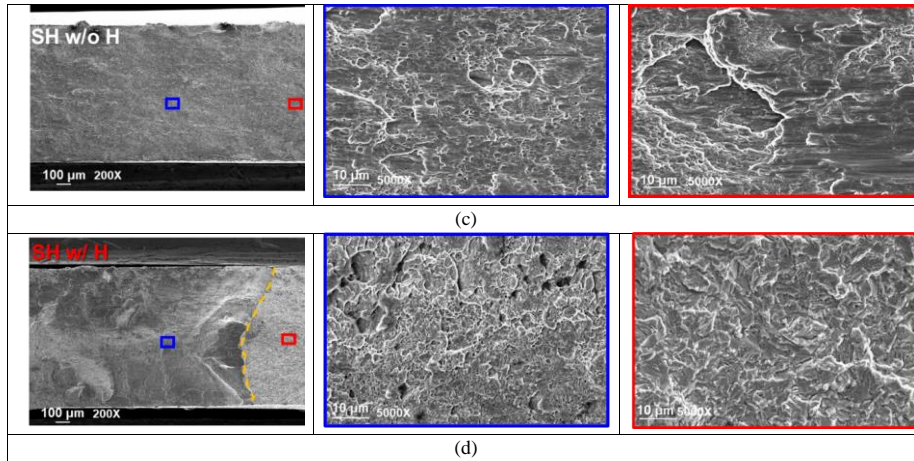


Fig. 12 Tensile fractography in edge site: (a-b) near the hole of CHD4 specimens without and with hydrogen charging, and (c-d) near the shear grooves of SH specimens without and with hydrogen charging.

In general, HE phenomenon is obviously found for all types of specimens of CP1000 steel. In specific, both HELP and HEDE mechanisms play roles in the ductility reduction of the studied material. HELP acts on the material resulting in smaller and shallower dimples but unchanging the ductile fracture mode, as illustrated in the whole region of SDB and NDBR40, and inner regions of CHD4 and SH specimens. Meanwhile, HEDE acts on the material by showing up river flow patterns mixed with very shallow dimples, which leads to a fracture mode transition from the ductile to the quasi-cleavage, as illustrated in the edge regions of CHD4 and SH specimens. There is a hint that CI locations lying in the specimen or at the specimen's surface should be separately treated for in-situ hydrogen charging mechanical tests in the future.

5 Conclusions

In this study, the uniaxial tensile tests were operated for CP1000 steel sheet to investigate the hydrogen influence on tensile property under various stress states by experiments and simulations. The hydrogen is introduced into the material by an electrochemical method, and TDS technique is used to measure the pre-charged hydrogen concentration. The simulated and experimental results are combined to analyze crack initiation moment and locations for tensile fracture specimens with or without hydrogen charging. Moreover, experimental fractography investigation was carried out to reveal fracture mechanisms of CP1000 steel in each condition. There are some conclusions drawn in the following:

- HE tendency of CP1000 steel is affected by stress state variations, and various stress states induce quantitatively different weakness of tensile properties responding to hydrogen, especially the crack initiation plastic strain and the ductility.
- In hydrogen environment, the quasi-cleavage fracture mode occurs in the region around the critical initiation sites of SH and CHD4 specimens, while the ductile fracture mode is observed for SDB and NDBR40 specimens. Herein, HEDE and HELP are separately activated for specimens with different stress states.
- The crack initiation site movement for SH specimens from the center to the edge near shear grooves suggests non-uniform hydrogen concentration and distribution in the specimen. Herein, in-situ hydrogen charging procedure and stress triaxiality are supposed to arise hydrogen accumulation in the critical site, results in the shift of crack initiation location.
- In current designed geometries, two groups of specimens can be classified for the further in-situ hydrogen charging mechanical testing: SH and CHD4 specimens with crack initiation location at the edge site, SDB and NDB40 specimens with crack initiation location at the center site. The study of stress state influence on the hydrogen embrittlement should consider

the geometry-induced local H concentration difference.

Based on previous study, the microstructure-related damage mechanisms of CP1000 steel in hydrogen environment considering stress state effect will be investigated in the future, and new geometries should be elaborately designed, especially for SH specimens, to assure their steady stress state during the in-situ hydrogen charging loading. Furthermore, coupled hydrogen diffusion and ductile-cleavage damage models are necessary to develop to realize accurate prediction of CP1000 steel fracture loci for industrial applications.

Acknowledgments

The authors are thankful for the Thyssenkrupp Steel Europe AG, Germany and the Technology Industry 100th Anniversary Foundation, Finland (Teknoliateollisuuden 100-vuotissäätiö, grant number: 2165) for the materials supply as well as financial support.

References

1. Koyama, M., et al., *Overview of hydrogen embrittlement in high-Mn steels*. International Journal of Hydrogen Energy, 2017. **42**(17): p. 12706-12723.
2. Mallick, D., et al., *Study of Diffusible Behavior of Hydrogen in First Generation Advanced High Strength Steels*. Metals, 2021. **11**(5): p. 782.
3. Pundt, A. and R. Kirchheim, *Hydrogen in metals: microstructural aspects*. Annual Review of Materials Research, 2006. **36**(1): p. 555-608.
4. Hillier, E. and M. Robinson, *Hydrogen embrittlement of high strength steel electroplated with zinc-cobalt alloys*. Corrosion science, 2004. **46**(3): p. 715-727.
5. Mabho, N., et al., *Determination of diffusible and total hydrogen concentration in coated and uncoated steel using melt and solid extraction techniques: Part I*. Talanta, 2010. **82**(4): p. 1298-1305.
6. Depover, T., et al., *Evaluation of the hydrogen embrittlement susceptibility in DP steel under static and dynamic tensile conditions*. International Journal of Impact Engineering, 2019. **123**: p. 118-125.
7. Depover, T., E. Wallaert, and K. Verbeken, *Fractographic analysis of the role of hydrogen diffusion on the hydrogen embrittlement susceptibility of DP steel*. Materials Science and Engineering: A, 2016. **649**: p. 201-208.
8. Han, J., J.-H. Nam, and Y.-K. Lee, *The mechanism of hydrogen embrittlement in intercritically annealed medium Mn TRIP steel*. Acta Materialia, 2016. **113**: p. 1-10.
9. Zhu, X., et al., *Effects of cryogenic and tempered treatment on the hydrogen embrittlement susceptibility of TRIP-780 steels*. International journal of hydrogen energy, 2013. **38**(25): p. 10694-10703.
10. Bai, Y., et al., *Effect of grain refinement on hydrogen embrittlement behaviors of high-Mn TWIP steel*. Materials Science and Engineering: A, 2016. **651**: p. 935-944.
11. Koyama, M., E. Akiyama, and K. Tsuzaki, *Hydrogen embrittlement in a Fe-Mn-C ternary twinning-induced plasticity steel*. Corrosion Science, 2012. **54**: p. 1-4.
12. Kolk, M.L.O., *Hydrogen embrittlement in HSSs limits use in lightweight body in white design*. Advanced Materials & Processes, 2011. **169**(3): p. 22-26.
13. Rudomilova, D., T. Prošek, and G. Luckeneder, *Techniques for investigation of hydrogen embrittlement of advanced high strength steels*. Corrosion Reviews, 2018. **36**(5): p. 413-434.

14. Peet, M.J., et al., *Strength and toughness of clean nanostructured bainite*. Materials Science and Technology, 2017. **33**(10): p. 1171-1179.
15. Song, W., et al., *Atomic-scale investigation of ϵ and θ precipitates in bainite in 100Cr6 bearing steel by atom probe tomography and ab initio calculations*. Acta Materialia, 2013. **61**(20): p. 7582-7590.
16. Frómeta, D., et al., *Fracture Resistance of Advanced High-Strength Steel Sheets for Automotive Applications*. Metallurgical and Materials Transactions A, 2021. **52**(2): p. 840-856.
17. Hwang, A.I., et al., *Influence of Microstructure Constituents on the Hydrogen - Induced Mechanical Degradation in Ultra - High Strength Sheet Steels*. Metals and Materials International, 2021. **27**(10): p. 3959-3967.
18. Drexler, A., et al., *On the local evaluation of the hydrogen susceptibility of cold-formed and heat treated advanced high strength steel (AHSS) sheets*. Materials Science and Engineering: A, 2021. **800**: p. 140276.
19. Malitckii, E., Y. Yagodzinskyy, and P. Vilaça, *Role of retained austenite in hydrogen trapping and hydrogen-assisted fatigue fracture of high-strength steels*. Materials Science and Engineering: A, 2019. **760**: p. 68-75.
20. Ahn, D.C., P. Sofronis, and R.H. Dodds, *On hydrogen-induced plastic flow localization during void growth and coalescence*. International Journal of Hydrogen Energy, 2007. **32**(16): p. 3734-3742.
21. Robertson, I.M., *The effect of hydrogen on dislocation dynamics*. Engineering Fracture Mechanics, 1999. **64**(5): p. 649-673.
22. Birnbaum, H.K. and P. Sofronis, *Hydrogen-enhanced localized plasticity—a mechanism for hydrogen-related fracture*. Materials Science and Engineering: A, 1994. **176**(1): p. 191-202.
23. Sun, B., et al., *Dependence of hydrogen embrittlement mechanisms on microstructure-driven hydrogen distribution in medium Mn steels*. Acta Materialia, 2020. **183**: p. 313-328.
24. Guzmán, A.A., et al., *Hydrogen embrittlement at cleavage planes and grain boundaries in bcc iron—revisiting the first-principles cohesive zone model*. Materials, 2020. **13**(24): p. 5785.
25. Dadfarnia, M., et al., *Recent advances on hydrogen embrittlement of structural materials*.

International Journal of Fracture, 2015. **196**(1): p. 223-243.

26. Oriani, R.A., *A mechanistic theory of hydrogen embrittlement of steels*. Berichte der Bunsengesellschaft für physikalische Chemie, 1972. **76**(8): p. 848-857.
27. Lin, M., et al., *A predictive model unifying hydrogen enhanced plasticity and decohesion*. Scripta Materialia, 2022. **215**: p. 114707.
28. Loidl, M., et al., *Characterization of hydrogen embrittlement in automotive advanced high strength steels*. Materialwissenschaft und Werkstofftechnik, 2011. **42**(12): p. 1105-1110.
29. Venezuela, J., et al., *The influence of microstructure on the hydrogen embrittlement susceptibility of martensitic advanced high strength steels*. Materials Today Communications, 2018. **17**: p. 1-14.
30. Koyama, M., et al., *Hydrogen-assisted decohesion and localized plasticity in dual-phase steel*. Acta Materialia, 2014. **70**: p. 174-187.
31. Zhu, X., et al., *Effect of retained austenite stability and morphology on the hydrogen embrittlement susceptibility in quenching and partitioning treated steels*. Materials Science and Engineering: A, 2016. **658**: p. 400-408.
32. Jemblie, L., V. Olden, and O.M. Akselsen, *A coupled diffusion and cohesive zone modelling approach for numerically assessing hydrogen embrittlement of steel structures*. International Journal of Hydrogen Energy, 2017. **42**(16): p. 11980-11995.
33. Huang, S., et al., *Fracture strain model for hydrogen embrittlement based on hydrogen enhanced localized plasticity mechanism*. international journal of hydrogen energy, 2020. **45**(46): p. 25541-25554.
34. Díaz, A., J.M. Alegre, and I.I. Cuesta, *Numerical simulation of hydrogen embrittlement and local triaxiality effects in notched specimens*. Theoretical and Applied Fracture Mechanics, 2017. **90**: p. 294-302.
35. Bal, B., et al., *Effect of hydrogen on fracture locus of Fe–16Mn–0.6C–2.15Al TWIP steel*. International Journal of Hydrogen Energy, 2020. **45**(58): p. 34227-34240.
36. Nguyen, T.T., et al., *Ductility and fatigue properties of low nickel content type 316L austenitic stainless steel after gaseous thermal pre-charging with hydrogen*. International Journal of Hydrogen Energy, 2019. **44**(51): p. 28031-28043.
37. Briottet, L., I. Moro, and P. Lemoine, *Quantifying the hydrogen embrittlement of pipeline steels for safety considerations*. International Journal of Hydrogen Energy, 2012. **37**(22):

p. 17616-17623.

38. Barthélémy, H., *Effects of pressure and purity on the hydrogen embrittlement of steels*. International Journal of Hydrogen Energy, 2011. **36**(3): p. 2750-2758.
39. Bai, Y. and T. Wierzbicki, *Forming severity concept for predicting sheet necking under complex loading histories*. International Journal of Mechanical Sciences, 2008. **50**(6): p. 1012-1022.
40. Bao, Y. and T. Wierzbicki, *On fracture locus in the equivalent strain and stress triaxiality space*. International Journal of Mechanical Sciences, 2004. **46**(1): p. 81-98.
41. Nahshon, K. and J.W. Hutchinson, *Modification of the Gurson Model for shear failure*. European Journal of Mechanics a-Solids, 2008. **27**(1): p. 1-17.
42. Nielsen, K.L. and V. Tvergaard, *Ductile shear failure or plug failure of spot welds modelled by modified Gurson model*. Engineering Fracture Mechanics, 2010. **77**(7): p. 1031-1047.
43. Lian, J., et al., *A hybrid approach for modelling of plasticity and failure behaviour of advanced high-strength steel sheets*. International Journal of Damage Mechanics, 2013. **22**(2): p. 188-218.
44. Sofronis, P. and R.M. McMeeking, *Numerical analysis of hydrogen transport near a blunting crack tip*. Journal of the Mechanics and Physics of Solids, 1989. **37**(3): p. 317-350.
45. Krom, A.H.M., R.W.J. Koers, and A. Bakker, *Hydrogen transport near a blunting crack tip*. Journal of the Mechanics and Physics of Solids, 1999. **47**(4): p. 971-992.
46. Fangnon, E., et al., *Determination of Critical Hydrogen Concentration and Its Effect on Mechanical Performance of 2200 MPa and 600 HBW Martensitic Ultra-High-Strength Steel*. Metals, 2021. **11**(6): p. 984.
47. Viyanit, E., *Numerical simulation of hydrogen assisted cracking in supermartensitic stainless steel welds*. 2005, Bundesanstalt für Materialforschung und-prüfung (BAM).
48. Bai, Y. and T. Wierzbicki, *A new model of metal plasticity and fracture with pressure and Lode dependence*. International Journal of Plasticity, 2008. **24**(6): p. 1071-1096.